Journal of
Mechanics of
Materials and Structures

THREE-DIMENSIONAL NONLINEAR ANALYSES OF SCARF REPAIR IN COMPOSITE LAMINATES AND SANDWICH PANELS

Manabendra Das, Erdogan Madenci and Damodar R. Ambur

Volume 3, Nº 9 November 2008

mathematical sciences publishers

JOURNAL OF MECHANICS OF MATERIALS AND STRUCTURES
Vol. 3, No. 9, 2008

THREE-DIMENSIONAL NONLINEAR ANALYSES OF SCARF REPAIR IN COMPOSITE LAMINATES AND SANDWICH PANELS

MANABENDRA DAS, ERDOGAN MADENCI AND DAMODAR R. AMBUR

A special-purpose analysis tool based on the finite element method is presented for parametric design studies of composite laminates and sandwich panels with scarf repairs. This design tool provides the complete three-dimensional stress and strain fields in scarf-repaired panels without any requirements on the nature of the lamination and the type of loading. The adherends are modeled using a plate element based on a higher-order single-layer theory, and the adhesive is modeled using a solid element. The higher-order nature of the plate theory makes it suitable for analyzing thick laminates and sandwich panels comprised of numerous plies. The model takes into account geometric nonlinearity in the adherends and assumes a bilinear stress-strain relationship for the adhesive. The responses of composite laminates with single- and double-sided repairs and sandwich panels with both full and partial repairs of the top face sheets are investigated.

1. Introduction

Bonded joints and repairs, in a variety of forms such as lap, step, and scarf, have become the most common types of repairs for composite laminated and sandwich panels. The objective of a scarf repair is to restore the static strength and durability of a composite structure that contains damage due to unexpected impact loading on the structure, crack occurrence within the structure after longtime use, and environmental reasons. Panels with scarf joints do not experience excessive secondary bending and the magnitude of transverse shear and peel stress concentration is not as severe as in lap and step joints. In fact in the case of homogeneous adherends, the stress variation inside the adhesive remains fairly uniform. In the case of panels made of composite laminates, however, a nonuniform stress variation inside the adhesive has been observed [Johnson 1989]. Therefore, a detailed analysis of composite laminates for the accurate prediction of the stress and strain fields becomes critical for failure analysis. Moreover, geometric nonlinearity due to adherend bending and material nonlinearity of the adhesive should be taken into account for realistic predictions. With the increasing use of sandwich panels in aircraft structures, the development of repair methods and analysis tools to investigate the responses of these panels with scarf repair has become very important [Tomblin et al. 2004].

Analytical and numerical methods have been used in the past to examine scarf joints [Hart-Smith 1973; Erdogan and Ratwani 1971]. These methods are two dimensional in nature and the scarf repair is analyzed based on a representative scarf joint. In a scarf joint, the entire load is transferred through the adhesive bond, as opposed to both the undamaged base material and the repair sharing the load in the case of a scarf repair. The two dimensional scarf joint model over-predicts the stresses inside the adhesive and therefore underestimates the strength of the repaired panel [Soutis and Hu 1997]. Moreover,

Keywords: scarf repair, laminate, sandwich panels, nonlinear analyses.

the adherends are assumed to be homogeneous, and arbitrary boundary conditions and loading cannot be imposed. More recently, Mortensen and Thomsen [1997] employed the classical plate theory to model the adherends and a nonlinear material model for the adhesive. The analysis permits adherend bending as well as arbitrary load and boundary conditions. Finite element analysis can be employed to overcome the limitations of the analytical methods. While comparing different finite element models for scarf repair analysis, Odi and Friend [2002] noticed that although a considerable amount of work had been done on bonded joints, the number of numerical analysis methods devoted to bonded repair was inadequate. Johnson [1989] carried out a finite element analysis of scarf joints to investigate the nonuniform stress variation in nonhomogeneous laminated composites. It was observed that due to discontinuity in adherend stiffness, the stress variation had an oscillating trend with peaks in the vicinity of the 0° plies. Similar characteristics were observed by Harman and Wang [2006], who carried out both analytical and finite element analyses to investigate the influence of a varying scarf angle on the shear stress distribution. Gunnion and Herszberg [2006] conducted two- and three-dimensional finite element analyses and investigated the influence of various parameters on the average and peak values of shear and peel stress. Their work was later extended to accommodate the elastic-plastic nature of the adhesive [Wang and Gunnion 2008]. Baker et al. [1999] carried out a combined experimental and computational analysis where a detailed three-dimensional finite element model was created and the tapered scarf was modeled as a series of steps. In several studies finite element models have been used to investigate the effect of scarf angle and stacking sequence on the failure load of panels with scarf repair [Du et al. 2004; Kumar et al. 2006; Campilho et al. 2007]. Very often, instead of discretizing each layer of the laminate, average material properties are utilized to represent a specific stacking sequence [Soutis and Hu 1997; Kumar et al. 2006]. This approach reduces the size of the model considerably but the oscillating variation of the stress field inside the adhesive layer is not captured. Although detailed three-dimensional finite element analyses of scarf joints using solid elements can be used to provide accurate results, these models tend to be computationally expensive due to the presence of the thin adhesive layer and the numerous layers of plies in the laminate or the face sheet of a sandwich panel. Mesh refinement can be significant, especially in the case of nonlinear analysis where a fine mesh might be required for convergence. Moreover, difficulties associated with parameterizing the meshing process requires extra effort in creating a new mesh every time a panel with a different number of plies, adhesive thicknesses, or panel dimensions is to be analyzed.

An alternative to this approach is to use an element based on a single-layer theory, which utilizes a modest number of degrees of freedom for the entire FE model and provides accurate results. The current analysis utilizes one such plate element [Das et al. 2005; Das et al. 2006] for the adherents and a separate solid element for the adhesive layer in between the adherents. The tapered scarf is modeled as a stepped joint with numerous steps in order to replicate the taper as closely as possible. The analysis incorporates geometric and material nonlinearity in the adherent and adhesive elements, respectively. A bilinear stress strain relationship is used for the material model and geometric nonlinearity is incorporated based on the total Lagrangian formulation. The model accounts for finite boundaries, the presence of a cutout or grind-out in the skin, general loading conditions, material anisotropy, different thicknesses of the repair patch and skin, and different repair and parent materials. The material properties are input for each ply without any limitation on refinement in the thickness direction. While it is computationally robust and fast, it leads to accurate stress predictions in each specific ply and the adhesive layer.

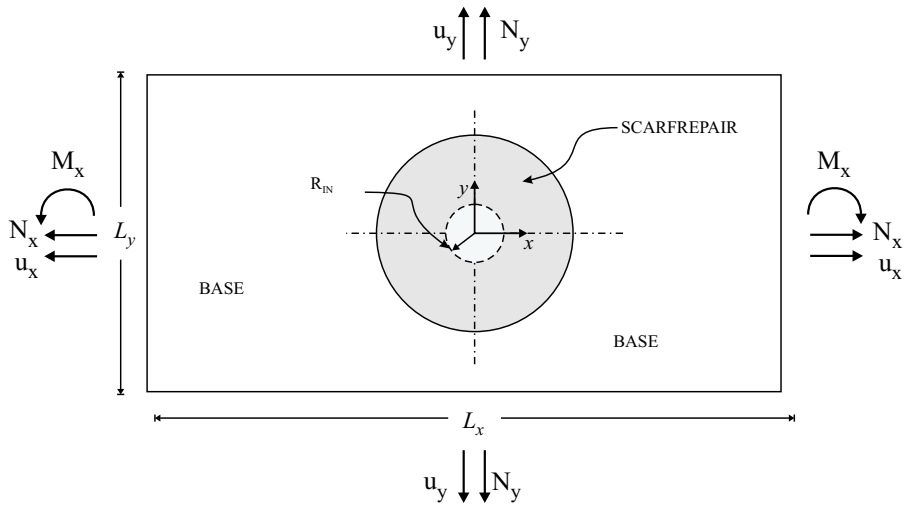

Figure 1. Top view of a panel with scarf repair under arbitrary loading conditions.

2. Problem definition

This study concerns the analysis of scarf repairs of composite laminates and sandwich panels. The top view of a composite laminate, or sandwich panel, with a scarf repair is illustrated in Figure 1. The panels have a rectangular geometry with length L_x and width L_y. As shown in Figure 1, the panel is subjected to forces, moments, and prescribed displacements at the edges. The composite laminate is made of several plies with orthotropic material properties. The laminate can have either a single-sided repair or a double-sided repair, as shown in Figures 2a and 2b. The sandwich panel can have either the full top face sheet or only a portion of it under the repair as shown in Figures 2c and 2d. The face sheets, as well as the core, can be composed of homogeneous, elastic, and orthotropic material layers. The problem posed herein concerns the determination of the complete three-dimensional stress and strain fields in the base and repair adherend and in the thin adhesive layer.

3. Present approach

The tapered scarf is modeled as a series of steps and each step consists of the adhesive layer in between the repair and base adherend. Plate elements, based on the {3,2}-order theory, and solid elements are utilized to model each step along the scarf repair. As shown in Figure 3, the base and repair adherends are represented through separate plate elements, through the thickness. The adhesive layer on the other hand is modeled using a solid element. Since all the plate elements are required to have a constant thickness, a fictitious material with a very low stiffness value is used in the region where the adherent does not occupy any space, as shown in Figure 3. A similar approach was adopted by Bair et al. [1991] for their FE model based on shell elements.

Since the nodes of the plate elements are placed along the mid-surface, they are not aligned with the nodes of the adhesive element. Hence, the nodes of the adhesive elements are offset to the mid-surface of the adherend elements so that they coincide with the nodes of the adherend element [Carpenter 1973]. The

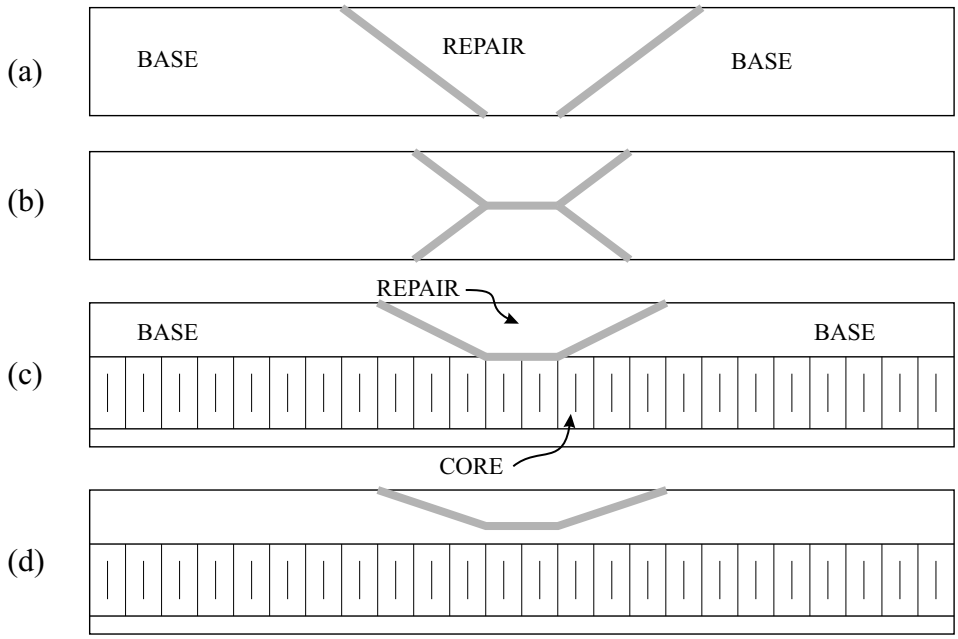

Figure 2. Side view of a composite panel with (a) single- and (b) double-sided repairs and a sandwich panel with (c) full repair of the top face sheet and (d) partial repair of the top face sheet.

details of the element formulation for the plate and solid elements are given in subsequent sections. The stiffness matrix and the unknown displacement vector of the super element, comprised of the adhesive and adherends, have the following forms

$$\boldsymbol{K}_{\text{SCARF}} = \begin{bmatrix} \boldsymbol{K}_b^P + \boldsymbol{K}_{bb}^S & \boldsymbol{K}_{br}^S \\ \boldsymbol{K}_{rb}^S & \boldsymbol{K}_r^P + \boldsymbol{K}_{rr}^S \end{bmatrix}_{78\times 78}, \qquad \boldsymbol{v}_{\text{SCARF}}^T = \left\{ \boldsymbol{v}_b^T \;\; \boldsymbol{v}_r^T \right\}, \tag{1}$$

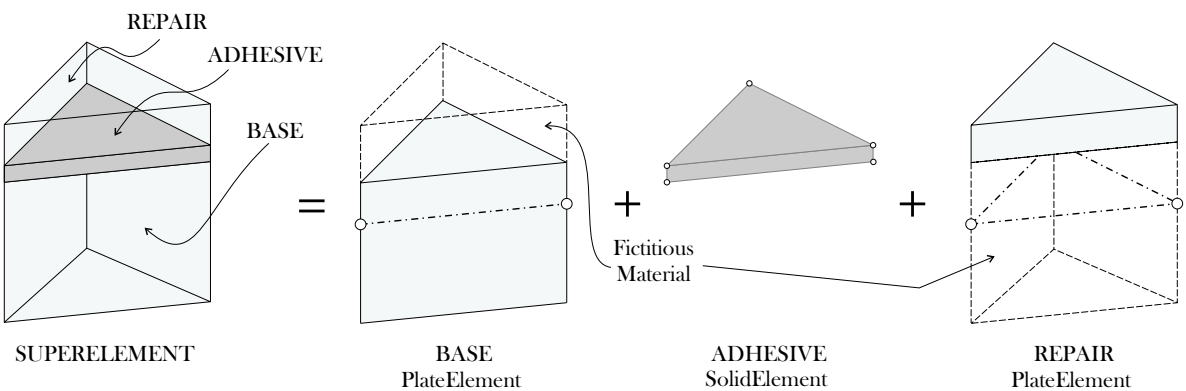

Figure 3. The scarf super element comprised of the two adherend plate elements with the solid adhesive element in between them.

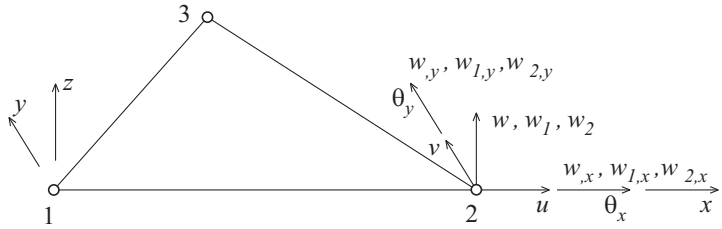

Figure 4. A triangular plate element with three nodes having 13 degrees of freedom at each node.

where $\boldsymbol{K}_b^P$ and $\boldsymbol{K}_r^P$ are the stiffness matrix of the base and repair adherend plate elements, respectively, and $\boldsymbol{K}^S$ corresponds to the stiffness matrix of the adhesive element. The displacement vector consists of the nodal unknowns, $\boldsymbol{v}_b$ and $\boldsymbol{v}_r$, that correspond to the base and repair plate elements, respectively. The region outside the repair zone is modeled using a single layer of plate elements.

4. Plate element

The plate element for the adherends is based on the {3,2}-order single-layer theory [Cook and Tessler 1998; Barut et al. 2001]. The triangular element contains 13 degrees of freedom at each node, as shown in Figure 4. These degrees of freedom consist of two in-plane displacements, (u, v), two out-of-plane rotations, (θ_x, θ_y), and three transverse nodal displacements, (w, w_1, w_2), and their derivatives, $(w_{,x}, w_{,y}, w_{1,x}, w_{1,y}, w_{2,x}, w_{2,y})$. The weighted-average in-plane displacement components in the x- and y-directions are denoted by u and v, respectively. The weighted-average transverse displacement is denoted by w. The weighted-average bending rotations about the negative x- and positive y-axes are denoted by θ_x and θ_y, respectively. Their positive sign convention is shown in Figure 4. The transverse displacements, not weighted-averaged, (w_1, w_2), represent the symmetric and antisymmetric expansion modes through the thickness of the element.

As shown by Barut et al. [2001], the displacement components of the plate are defined as

$$\begin{aligned} u_x(x, y, z) = u(x, y) + h\zeta\theta_y(x, y) + \left(\frac{1}{6} - \frac{\zeta^2}{2}\right) h w_{1,x}(x, y) \\ + h\left(\frac{\zeta}{5} - \frac{\zeta^3}{3}\right)\left[\frac{5}{4}\big(\theta_y(x, y) + w_{,x}(x, y)\big) + w_{2,x}(x, y)\right], \end{aligned} \tag{2a}$$

$$\begin{aligned} u_y(x, y, z) = v(x, y) + h\zeta\theta_x(x, y) + \left(\frac{1}{6} - \frac{\zeta^2}{2}\right) h w_{1,y}(x, y) \\ + h\left(\frac{\zeta}{5} - \frac{\zeta^3}{3}\right)\left[\frac{5}{4}\big(\theta_x(x, y) + w_{,y}(x, y)\big) + w_{2,y}(x, y)\right], \end{aligned} \tag{2b}$$

$$u_z(x, y, z) = w(x, y) + w_1(x, y)\zeta + w_2(x, y)(\zeta^2 - 1/5), \tag{2c}$$

where $\zeta = z/h$ is the normalized thickness and varies in the range $-1 \le \zeta \le 1$. In accordance with the {3,2} plate theory, the in-plane displacement components vary cubically and the transverse displacement

component varies quadratically across the thickness of the panel. At any point in the panel, the in-plane displacement components in the x- and y-directions are represented by $u_x(x, y, z)$ and $u_y(x, y, z)$, respectively, and the transverse displacement component by $u_z(x, y, z)$.

The definitions of the stress and moment resultants and the form of the resultant strain and curvatures are provided in [Barut et al. 2001]. The resultant stresses and moments are expressed in terms of the strain and curvature components as

$$\begin{Bmatrix} \boldsymbol{N} \\ \boldsymbol{M} \\ \boldsymbol{Q} \end{Bmatrix} = \begin{bmatrix} \boldsymbol{A} & \boldsymbol{B} & \boldsymbol{0} \\ \boldsymbol{B}^T & \boldsymbol{D} & \boldsymbol{0} \\ \boldsymbol{0} & \boldsymbol{0} & \boldsymbol{G} \end{bmatrix} \begin{Bmatrix} \boldsymbol{\epsilon} \\ \boldsymbol{\kappa} \\ \boldsymbol{\gamma} \end{Bmatrix}, \tag{3}$$

where

$$\boldsymbol{N}^T = \{N_{xx0}, N_{yy0}, N_{zz0}, N_{xy0}, N_{xx1}, N_{yy1}, N_{xy1}\}, \tag{4a}$$

$$\boldsymbol{M}^T = \{M_{xx0}, M_{yy0}, M_{zz0}, M_{xy0}, M_{xx1}, M_{yy1}, M_{xy1}\}, \tag{4b}$$

$$\boldsymbol{Q}^T = \{Q_{yz0}, Q_{xz0}\}, \tag{4c}$$

$$\boldsymbol{\epsilon}^T = \{\varepsilon_{xx0}, \varepsilon_{yy0}, \varepsilon_{zz0}, \gamma_{xy0}, \varepsilon_{xx1}, \varepsilon_{yy1}, \gamma_{xy1}\}, \tag{4d}$$

$$\boldsymbol{\kappa}^T = \{\kappa_{xx0}, \kappa_{yy0}, \kappa_{zz0}, \kappa_{xy0}, \kappa_{xx1}, \kappa_{yy1}, \kappa_{xy1}\}, \tag{4e}$$

$$\boldsymbol{\gamma}^T = \{\gamma_{yz0}, \gamma_{xz0}\}. \tag{4f}$$

The explicit forms of $\boldsymbol{A}$, $\boldsymbol{B}$, $\boldsymbol{D}$, and $\boldsymbol{G}$ are given in [Barut et al. 2001]. This constitutive relation can also be expressed in terms of the compliance matrix $\boldsymbol{C}$ in the form $\boldsymbol{E} = \boldsymbol{C}\boldsymbol{S}$, where $\boldsymbol{E}^T = \{\boldsymbol{\epsilon}^T \ \ \boldsymbol{\kappa}^T \ \ \boldsymbol{\gamma}^T\}$ and $\boldsymbol{S}^T = \{\boldsymbol{N}^T \ \ \boldsymbol{M}^T \ \ \boldsymbol{Q}^T\}$. The governing equations concerning the equilibrium equations and continuity of interelement displacements along the element edges are derived utilizing the principle of virtual work. The resulting equations of equilibrium and boundary conditions are derived in [Barut et al. 2001]. The kinematic continuity conditions are imposed not only on the weighted-average displacements and slopes, $(u, v, w, \theta_x, \theta_y)$, but also on the derivatives of the higher-order displacement modes, (w_1, w_2), in the transverse direction. Therefore, the finite element implementation of the equilibrium equations requires at least C^1 interelement continuity for the out-of-plane displacement modes of w, w_1, and w_2. Because of this requirement, the finite element implementation of the total potential energy functional in terms of the assumed displacement field becomes rather difficult. The hybrid energy functional formulation overcomes the difficulty of the C^1 interelement continuity requirement because the displacements, as well as the slopes, are independently assumed only along element boundaries, which can be rendered identical along the common boundaries of adjacent elements. However, the kinematic compatibility between the displacements and slopes along the element boundaries is preserved in order to avoid a possible shear-locking phenomenon. Also, as part of the hybrid energy functional formulation, the stress and moment resultants within the element are selected such that they satisfy the equilibrium equations.

The hybrid energy functional for an element, Π_H, is defined as

$$\Pi_H = \frac{1}{2}\int_{A_e} \boldsymbol{S}^T \boldsymbol{C}\boldsymbol{S}\, dA - \int_{\Gamma_e} \boldsymbol{T}_b^T \boldsymbol{u}_b\, d\Gamma, \tag{5}$$

in which the element boundary is denoted by Γ_e and its area by A_e. The vectors $\boldsymbol{T}_b$ and $\boldsymbol{u}_b$ include the components of the boundary forces and boundary displacements, respectively. In accordance with the hybrid energy formulation, the resultant stress vector, $\boldsymbol{S}$, must satisfy the equilibrium equations identically. The derivation of the resultant stress vector, $\boldsymbol{S}$, satisfying the equilibrium equations is presented in [Das et al. 2005]. Also, the boundary displacement vector, $\boldsymbol{u}_b^{(k)}$, containing the assumed boundary displacement components, and the boundary stress vector, $\boldsymbol{T}_b^{(k)}$, containing the resultant stresses and moments corresponding to the boundary displacement vector $\boldsymbol{u}_b^{(k)}$, are given in [Das et al. 2005]. Substituting for the stress vector, the boundary displacement and boundary stress vectors in the hybrid energy functional result in

$$\Pi_H = \tfrac{1}{2}\boldsymbol{b}^T\boldsymbol{H}\boldsymbol{b} + \boldsymbol{\lambda}^T\boldsymbol{c}\boldsymbol{b} + \boldsymbol{R}_b^T\boldsymbol{b} - \boldsymbol{R}_v^T\boldsymbol{v} - \boldsymbol{b}^T\boldsymbol{G}\boldsymbol{v} + \Pi_0, \tag{6}$$

where

$$\begin{gathered}\boldsymbol{H} = \int_{A_e} \boldsymbol{P}^T\boldsymbol{C}\boldsymbol{P}\,dA, \qquad \boldsymbol{G} = \sum_k \int_{\Gamma_{(k)}} \boldsymbol{P}^T\boldsymbol{B}_s^{(k)}\boldsymbol{B}_b^{(k)}\boldsymbol{L}^{(k)}\,d\Gamma, \\ \boldsymbol{R}_b = \int_{A_e} \boldsymbol{S}_0^T\boldsymbol{C}\boldsymbol{P}\,dA, \qquad \boldsymbol{R}_v = \sum_{k=1}^{3} \int_{\Gamma_{(k)}} \boldsymbol{S}_0^T\boldsymbol{B}_s^{(k)}\boldsymbol{B}_b^{(k)}\boldsymbol{L}^{(k)}\,d\Gamma, \qquad \Pi_0 = \frac{1}{2}\int_{A_e} \boldsymbol{S}_0^T\boldsymbol{C}\boldsymbol{S}_0\,dA,\end{gathered} \tag{7}$$

in which the explicit definition of each of the matrices and vectors is given in [Das et al. 2005]. In matrix form, the hybrid energy functional, Π_H, can be rewritten as

$$\Pi_H = \tfrac{1}{2}\hat{\boldsymbol{b}}^T\hat{\boldsymbol{H}}\hat{\boldsymbol{b}} + \hat{\boldsymbol{R}}_b^T\hat{\boldsymbol{b}} - \boldsymbol{R}_v^T\boldsymbol{v} + \hat{\boldsymbol{b}}^T\hat{\boldsymbol{G}}\boldsymbol{v} + \Pi_0, \tag{8}$$

where

$$\hat{\boldsymbol{b}}^T = \{\boldsymbol{b}^T, \boldsymbol{\lambda}^T\}, \qquad \hat{\boldsymbol{H}} = \begin{bmatrix}\boldsymbol{H} & \boldsymbol{c}^T \\ \boldsymbol{c} & \boldsymbol{0}\end{bmatrix}, \qquad \hat{\boldsymbol{R}}_b^T = \{\boldsymbol{R}_b^T, \boldsymbol{0}^T\}, \qquad \hat{\boldsymbol{G}} = \begin{bmatrix}\boldsymbol{G} \\ \boldsymbol{0}\end{bmatrix}.$$

In accordance with the concept of energy minimization, the first variation of the hybrid energy functional with respect to the unknown vector $\hat{\boldsymbol{b}}$ of generalized coordinates yields

$$\delta\hat{\boldsymbol{b}}^T\left(\hat{\boldsymbol{H}}\hat{\boldsymbol{b}} + \hat{\boldsymbol{R}}_b - \hat{\boldsymbol{G}}\boldsymbol{v}\right) = \boldsymbol{0} \qquad \text{or} \qquad \hat{\boldsymbol{b}} = \hat{\boldsymbol{H}}^{-1}\left(\hat{\boldsymbol{G}}\boldsymbol{v} - \hat{\boldsymbol{R}}_b\right). \tag{9}$$

With this explicit solution form, the hybrid energy functional becomes

$$\Pi_H = -\tfrac{1}{2}\boldsymbol{v}^T\boldsymbol{k}_L\boldsymbol{v} + \boldsymbol{f}_0^T\boldsymbol{v} + \Pi_0, \tag{10}$$

in which the linear stiffness matrix $\boldsymbol{k}_L$ and the resultant force (load) vector $\boldsymbol{f}_0$ are defined as

$$\boldsymbol{k}_L = \hat{\boldsymbol{G}}^T\hat{\boldsymbol{H}}^{-1}\hat{\boldsymbol{G}} \qquad \text{and} \qquad \boldsymbol{f}_0^T = \hat{\boldsymbol{R}}_b^T\hat{\boldsymbol{H}}^{-1}\hat{\boldsymbol{G}} - \hat{\boldsymbol{R}}_v^T. \tag{11}$$

Finally, the element equilibrium equation is obtained by requiring the first variation of the hybrid energy functional to vanish

$$\delta\Pi_H = \delta\boldsymbol{v}^T(\boldsymbol{k}_L\boldsymbol{v} - \boldsymbol{f}_0) = 0. \tag{12}$$

For arbitrary variation of $\delta\boldsymbol{v}$, the element equilibrium equations become

$$\boldsymbol{k}_L\boldsymbol{v} = \boldsymbol{f}_0. \tag{13}$$

The nonlinear analysis is based on the total Lagrangian formulation. The principle of virtual work in the total Lagrangian formulation is given by

$$\int_{0V} \sum_k {}_0^{t+\Delta t}S^{(k)} \delta_0 E^{(k)} d^0V = \delta^{t+\Delta t}\Re. \tag{14}$$

In this expression, the left subscript indicates the configuration by which the quantity is measured and the left superscript refers to the configuration of the body at a specific time. The right superscript refers to the kth component of the Piola-Kirchoff stress, $\boldsymbol{S}$, and Green strain, $\boldsymbol{E}$, resultant vector. The right-hand side of Equation (14) represents the virtual work done by the conservative external forces on the virtual displacements. The Piola-Kirchoff stress are decomposed between times t and $t+\Delta t$ as

$${}_0^{t+\Delta t}S^{(k)} = {}_0^{t}S^{(k)} + {}_0S^{(k)}. \tag{15}$$

The incremental Piola-Kirchoff stress vector, ${}_0S^{(k)}$, represents the incremental loading between $t+\Delta t$ and t, and ${}_0^{t}S^{(k)}$ represents the known component from time t. The Green strain at any state $t+\Delta t$ can be written in terms of linear and nonlinear components as

$${}_0^{t+\Delta t}E^{(k)} = {}_0^{t+\Delta t}E_L^{(k)} + {}_0^{t+\Delta t}E_{NL}^{0}. \tag{16}$$

This expression can be written in terms of the unknown displacement as

$${}_0^{t+\Delta t}E^{(k)} = \boldsymbol{B}_L^{(k)^T}\left({}^t\boldsymbol{v}+\boldsymbol{v}\right) + \tfrac{1}{2}\left({}^t\boldsymbol{v}+\boldsymbol{v}\right)^T \boldsymbol{B}_{NL}^{(k)}\left({}^t\boldsymbol{v}+\boldsymbol{v}\right), \tag{17}$$

where $\boldsymbol{B}_L^{(k)}$ and $\boldsymbol{B}_{NL}^{(k)}$ are the linear and nonlinear strain-displacement relationship vector and matrix, respectively, corresponding to the kth strain resultant component. Based on the hybrid formulation, the linear strain-displacement relationship matrix can be expressed as

$$\boldsymbol{B}_L = \boldsymbol{C}\boldsymbol{P}\hat{\boldsymbol{H}}^{-1}\hat{\boldsymbol{G}}. \tag{18}$$

The matrix $\boldsymbol{B}_{NL}^{(k)}$ is obtained based on von Karman assumptions and therefore the current analysis is applicable only for small rotations. The incremental strain ${}_0E^{(k)}$ can be obtained by finding the difference between the strain at state $t+\Delta t$ and t

$${}_0E^{(k)} = {}_0^{t+\Delta t}E^{(k)} - {}_0^{t}E^{(k)} = \boldsymbol{B}_L^{(k)^T}\boldsymbol{v} + {}^t\boldsymbol{v}^T\boldsymbol{B}_{NL}^{(k)}\boldsymbol{v} + \tfrac{1}{2}\boldsymbol{v}^T\boldsymbol{B}_{NL}^{(k)}\boldsymbol{v}. \tag{19}$$

The virtual strain increment can be expressed as

$$\delta_0E^{(k)} = \boldsymbol{B}_L^{(k)^T}\delta\boldsymbol{v} + {}^t\boldsymbol{v}^T\boldsymbol{B}_{NL}^{(k)}\delta\boldsymbol{v} + \boldsymbol{v}^T\boldsymbol{B}_{NL}^{(k)}\delta\boldsymbol{v}. \tag{20}$$

Based on Equations (15) and (19), the expression for stress can now be written in terms of the unknown displacements as

$${}_0^{t+\Delta t}S^{(k)} = {}_0^{t}S^{(k)} + \sum_j C_{jk}^{-1}E^{(j)} = {}_0^{t}S^{(k)} + \sum_j C_{jk}^{-1}\left(\boldsymbol{B}_L^{(j)^T}\boldsymbol{v} + {}^t\boldsymbol{v}^T\boldsymbol{B}_{NL}^{(j)}\boldsymbol{v} + \tfrac{1}{2}\boldsymbol{v}^T\boldsymbol{B}_{NL}^{(j)}\boldsymbol{v}\right), \tag{21}$$

where C_{jk}^{-1} represents the linear relationship between the resultant stresses and strains. Substituting the expressions for virtual incremental strain and total stress from Equations (20) and (21) into the virtual

work expression and neglecting the higher order terms results in

$$\left(\int_{0V}\left(\sum_k\sum_j \boldsymbol{B}_L^{(k)}C_{jk}^{-1}\boldsymbol{B}_L^{(k)^T}+\sum_k\sum_j \boldsymbol{B}_L^{(k)}C_{jk}^{-1\,t}\boldsymbol{v}^T\boldsymbol{B}_{NL}^{(k)}+\sum_k \boldsymbol{B}_{NL}^{(k)\,t}\boldsymbol{v}C_{jk}^{-1\,t}\boldsymbol{B}_L^{(k)^T}\right.\right.$$
$$\left.\left.+\sum_k \boldsymbol{B}_{NL}^{(k)\,t}\boldsymbol{v}C_{jk}^{-1\,t}\boldsymbol{v}^T\boldsymbol{B}_{NL}^{(k)}+\sum_k {}_0^tS^{(k)}\boldsymbol{B}_{NL}^{(k)}\right)d^0V\right)\boldsymbol{v}=\boldsymbol{f}_e-\sum_k {}_0^tS^{(k)}\boldsymbol{B}_L^{(k)}-\sum_k {}_0^tS^{(k)}\boldsymbol{B}_{NL}^{(k)\,t}\boldsymbol{v}. \quad (22)$$

The final nonlinear system of finite element equations can be written as

$$\boldsymbol{K}^P\boldsymbol{v}=\boldsymbol{F}^P, \quad (23)$$

where $\boldsymbol{K}^P=\boldsymbol{k}_L+\boldsymbol{k}_v+\boldsymbol{k}_\sigma$ and ${}^P\boldsymbol{F}=\boldsymbol{f}_e-\boldsymbol{f}_i$. The matrices $\boldsymbol{k}_L$, $\boldsymbol{k}_v$, and $\boldsymbol{k}_\sigma$ are the linear, initial displacement, and geometric stiffness matrices, respectively, and $\boldsymbol{f}_i$ and $\boldsymbol{f}_e$ are the internal and external force vectors, respectively. The explicit form of these matrices and vectors is as follows

$$\boldsymbol{k}_L=\int_{0V}\left(\sum_k\sum_j \boldsymbol{B}_L^{(k)}C_{jk}^{-1}\boldsymbol{B}_L^{(k)^T}\right)d^0V, \quad (24a)$$

$$\boldsymbol{k}_v=\int_{0V}\left(\sum_k\sum_j \boldsymbol{B}_L^{(k)}C_{jk}^{-1}\boldsymbol{v}^T\boldsymbol{B}_{NL}^{(k)}+\sum_k \boldsymbol{B}_{NL}^{(k)\,t}\boldsymbol{v}C_{jk}^{-1\,t}\boldsymbol{B}_L^{(k)^T}+\sum_k \boldsymbol{B}_{NL}^{(k)\,t}\boldsymbol{v}C_{jk}^{-1\,t}\boldsymbol{v}^T\boldsymbol{B}_{NL}^{(k)}\right)d^0V, \quad (24b)$$

$$\boldsymbol{k}_\sigma=\int_{0V}\left(\sum_k {}_0^tS^{(k)}\boldsymbol{B}_{NL}^{(k)}\right)d^0V, \quad (24c)$$

$$\boldsymbol{f}_i=\int_{0V}\left(\sum_k {}_0^tS^{(k)}\boldsymbol{B}_L^{(k)}+\sum_k {}_0^tS^{(k)}\boldsymbol{B}_{NL}^{(k)\,t}\boldsymbol{v}\right)d^0V. \quad (24d)$$

Note that by combining the linear strain-displacement relationship matrix given in Equation (18) with Equation (24a), the linear stiffness matrix obtained from the hybrid formulation, Equation (11), can be reproduced.

5. Adhesive element

A solid element with six nodes is used for the adhesive layer. Unlike the plate element, the adhesive element is based on a displacement formulation and each node has three degrees of freedom. The displacement field varies linearly both in the in-plane and transverse directions. Therefore, the displacement field inside the adhesive can be expressed as

$$\boldsymbol{u}^S=\begin{bmatrix}\boldsymbol{N}_{\eta+} & \boldsymbol{0}\\ \boldsymbol{0} & \boldsymbol{N}_{\eta-}\end{bmatrix}\begin{bmatrix}\boldsymbol{N}_{xy} & \boldsymbol{0}\\ \boldsymbol{0} & \boldsymbol{N}_{xy}\end{bmatrix}\begin{Bmatrix}\boldsymbol{v}_{\text{bot}}^S\\ \boldsymbol{v}_{\text{top}}^S\end{Bmatrix}, \quad (25)$$

where $\boldsymbol{u}^S=\{u_x^S\ u_y^S\ u_z^S\}^T$ and $\boldsymbol{v}_{\text{bot}}^S$ and $\boldsymbol{v}_{\text{top}}^S$ consist of the nodal displacements corresponding to the bottom and top surfaces, respectively. As mentioned earlier, the nodes of the solid element do not coincide with the nodes of the adherend plate element. Therefore, in order to enforce continuity, the nodes of the adhesive elements are offset to the mid-surface of the adherend elements. The displacements at the nodes of the solid element are expressed in terms of the nodal displacements of the plate element, as

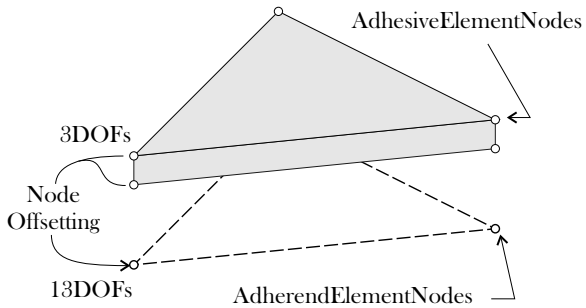

Figure 5. Offset nodes of the solid element for the adhesive.

shown in Figure 5, based on the following transformation

$$\begin{Bmatrix} \boldsymbol{v}^S_{\text{bot}} \\ \boldsymbol{v}^S_{\text{top}} \end{Bmatrix} = \begin{bmatrix} \boldsymbol{T}_b & \boldsymbol{0} \\ \boldsymbol{0} & \boldsymbol{T}_r \end{bmatrix} \begin{Bmatrix} \boldsymbol{v}^P_b \\ \boldsymbol{v}^P_r \end{Bmatrix}, \tag{26}$$

where $\boldsymbol{v}^P_b$ and $\boldsymbol{v}^P_r$ are nodal displacements of the base and repair plate element, and $\boldsymbol{T}_b$ and $\boldsymbol{T}_r$ are transformation matrices. The transformation matrices are constructed based on the definition of through-the-thickness variation of the displacement field inside the adherend plate, as given in Equation (2). Combining Equations (25) and (26), the displacement field inside the adhesive element can now be expressed in terms of the degrees of freedom associated with the plate elements as

$$\boldsymbol{u}^S = \begin{bmatrix} \boldsymbol{N}_{\eta+} & \boldsymbol{0} \\ \boldsymbol{0} & \boldsymbol{N}_{\eta-} \end{bmatrix} \begin{bmatrix} \boldsymbol{N}_{xy} & \boldsymbol{0} \\ \boldsymbol{0} & \boldsymbol{N}_{xy} \end{bmatrix} \begin{bmatrix} \boldsymbol{T}^{(i)} & \boldsymbol{0} \\ \boldsymbol{0} & \boldsymbol{T}^{(j)} \end{bmatrix} \begin{Bmatrix} \boldsymbol{v}^P_b \\ \boldsymbol{v}^P_r \end{Bmatrix}. \tag{27}$$

Using the displacement variation given in Equation (27), the strain field inside the element takes the form

$$\boldsymbol{\varepsilon}^S = \boldsymbol{B}^S \begin{Bmatrix} \boldsymbol{v}^P_b \\ \boldsymbol{v}^P_r \end{Bmatrix}, \tag{28}$$

where $\boldsymbol{B}^S$ is the strain-displacement transformation matrix. Instead of using a typical shear lag model, the adhesive layer takes into account the presence of all six components of strain such that

$$\boldsymbol{\varepsilon}^S = \{\varepsilon_{xx} \;\; \varepsilon_{yy} \;\; \varepsilon_{zz} \;\; \gamma_{yz} \;\; \gamma_{xz} \;\; \gamma_{xy}\}^T. \tag{29}$$

The stiffness matrix is therefore defined as

$$\boldsymbol{K}^S = \int_{S_V} \boldsymbol{B}^{S^T} \boldsymbol{D}^S \boldsymbol{B}^S dV = \begin{bmatrix} \boldsymbol{K}^S_{bb} & \boldsymbol{K}^S_{br} \\ \boldsymbol{K}^S_{rb} & \boldsymbol{K}^S_{rr} \end{bmatrix}_{78\times 78}, \tag{30}$$

where $\boldsymbol{D}^S$ is the stress-strain relationship matrix. The isotropic adhesive material has a bilinear relation between the effective transverse shear stress, τ_{eff}, and effective transverse shear strain, γ_{eff}. The effective transverse shear stress and strain in the adhesive are defined as

$$\tau_{\text{eff}} = \sqrt{\tau^2_{xz} + \tau^2_{yz}} \tag{31a}$$

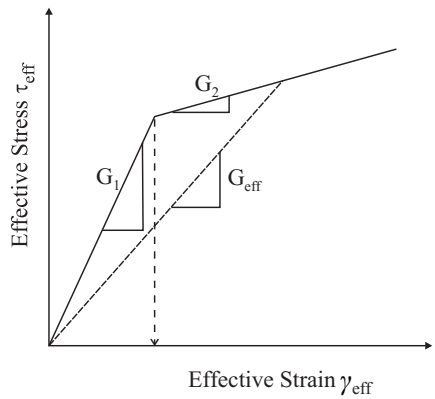

Figure 6. Bilinear relationship between effective stress and strain.

and

$$\gamma_{\text{eff}} = \sqrt{\gamma_{xz}^2 + \gamma_{yz}^2}. \tag{31b}$$

As shown in Figure 6, the initial shear modulus of the bilinear adhesive behavior is denoted by G_1, and it reduces to G_2 when the effective transverse shear strain, γ_{eff}, reaches the critical shear strain, γ_c. For a given value of effective shear strain, the effective shear stress can be obtained from Figure 6. Thereafter, the effective shear modulus can be obtained as

$$G_{\text{eff}} = \tau_{\text{eff}}/\gamma_{\text{eff}}. \tag{32}$$

Moreover, the effective Young's modulus can be expressed as

$$E_{\text{eff}} = 2G_{\text{eff}}(1+\nu). \tag{33}$$

Note that due to the dependence of the effective modulus on the effective strain, the system of equations become nonlinear.

6. Results and discussion

The current analysis tool is validated against an analytical solution and the commercial finite element analysis software ANSYS. Although both two-dimensional and three-dimensional models were created using ANSYS, only the three-dimensional results are reported here. In the ANSYS model, two layers of elements were used for each ply in the adherends and the adhesive was divided into three layers of elements. PLANE 42 and SOLID 45 elements were used for the two-dimensional and three-dimensional model, respectively. Similar to the approximation made in the current analysis tool, a series of steps were used to represent the scarf, instead of modeling it as a smooth taper. The adhesive along with each ply in the laminate was divided into multiple steps and one layer of solid element was used for every step.

The first problem involves the linear analysis of a two-dimensional scarf joint previously considered by [Erdogan and Ratwani 1971]. The scarf joint is subjected to in-plane stress, and its geometry is shown in Figure 7. The first adherend is made of aluminum with an elastic modulus $E = 1.0 \times 10^7$ psi and Poisson's ratio $\nu = 0.3$. The second adherend is made of boron-epoxy with elastic moduli $E_x = 3.24 \times 10^7$ psi and $E_z = 3.5 \times 10^6$ psi, shear modulus $G = 1.23 \times 10^6\ psi$, and Poisson's ratio $\nu_x = 0.23$. An epoxy

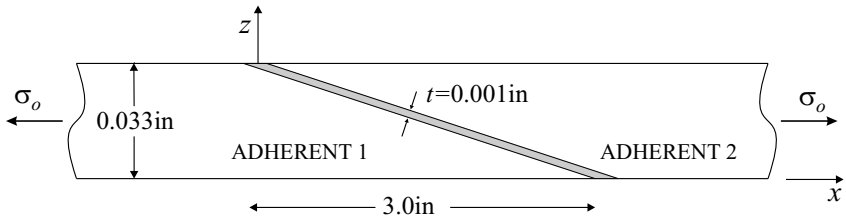

Figure 7. Schematics of the scarf joint.

material with elastic modulus $E = 4.45 \times 10^5$ psi and shear modulus $G = 1.65 \times 10^5$ psi is used for the thin adhesive layer. Since the analytical analysis does not permit the adherends to bend, for this problem, the bending deformations were suppressed in the finite element analysis as well. The transverse shear stress variation inside the adhesive layer is shown in Figure 8. Unlike a lap or step joint, the scarf joint has a fairly uniform variation of shear stress inside the adhesive. The difference in the results from the analytical and current finite element analysis is due to the presence of stress-free boundary condition at the edges. The current finite element solution tries to satisfy the stress boundary condition whereas the analytical results do not capture this feature.

The nonuniform variation of adhesive stress in a composite laminated joint is investigated next. The two-dimensional joint has a stacking sequence of $(45/90/-45/0)_5$, and each ply has a thickness of 0.0072 in. The total length of the panel is 12.32 in, and the scarf ratio is 30.0. The material properties of the plies in the base and repair adherends are given in Table 1. The 0.01-inch-thick adhesive has linear material properties with shear modulus $G = 6.0 \times 10^4$ psi and Poisson's ratio $\nu = 0.3$. The panel is subjected to an in-plane force of $N_x = 1000.0$ lbs/in; the stresses in the adhesive are shown in Figure 9. Unlike the homogeneous adherends, the stress distribution in the laminated joints has an oscillating trend and locations of the peaks are in the vicinity of the 0° degree plies. The transverse shear stress,

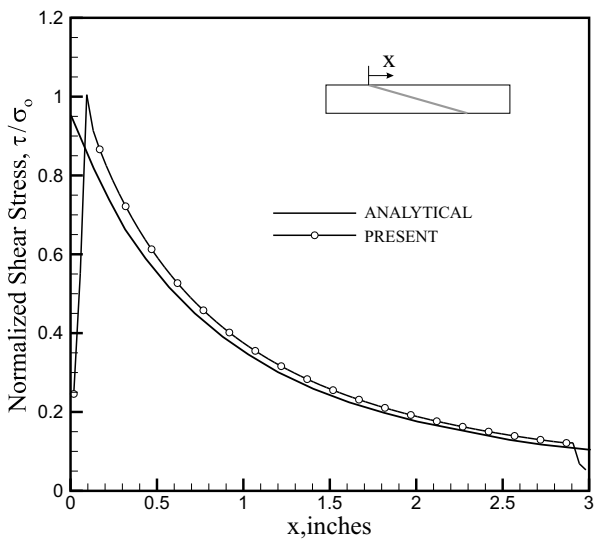

Figure 8. Shear stress variation inside the adhesive layer of a scarf joint.

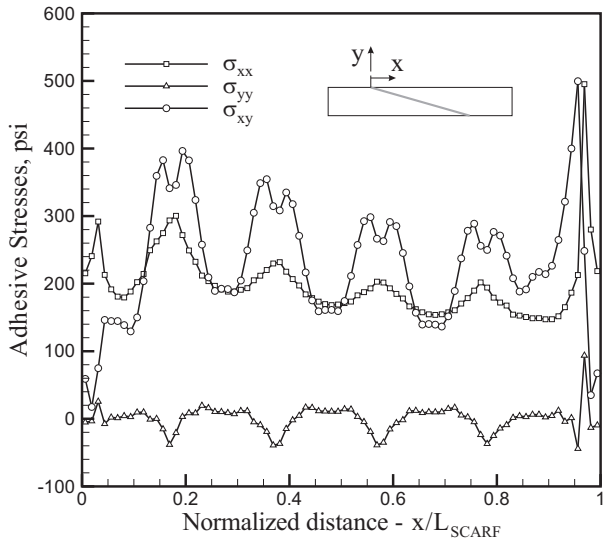

Figure 9. Stress variation inside the adhesive layer of a scarf joint.

σ_{xy}, is the dominant component whereas the magnitude of transverse normal stress, σ_{yy}, is much smaller even though the laminate has an unsymmetrical stacking sequence. Since the adhesive element is not based on a typical shear-lag-type model, the in-plane normal stress, σ_{xx}, can also be computed using the current analysis; the results are shown in Figure 9.

The next problem involves the three-dimensional scarf repair analysis of a composite laminate with a single-sided repair. The panel has length and width of 40 in and 28 in, respectively. The inner radius of the scarf repair is 0.25 in, and the scarf ratio is 30.0. The laminate has a stacking sequence of $(45/90/-45/0)_{5s}$, and each ply has a thickness of 0.0072 in. The adhesive thickness and material properties of the base, repair, and adhesive are the same as the scarf joint discussed earlier. The linear and geometrically nonlinear responses of the repaired laminate under two loading conditions have been analyzed. In the first case, a moment of $M_x = 10.0$ lbs-in/in is applied at the edges of the panel. The

	Base	Repair	Core
E_1(psi)	1.85×10^7	1.58×10^7	1.50×10^2
E_2(psi)	1.00×10^6	8.50×10^5	7.50×10^1
E_3(psi)	1.00×10^6	8.50×10^5	2.00×10^5
G_{12}(psi)	5.20×10^5	4.40×10^5	1.00×10^3
G_{13}(psi)	5.20×10^5	4.40×10^5	1.00×10^3
G_{23}(psi)	3.30×10^5	2.80×10^5	4.00×10^4
ν_{12}	0.34	0.34	1.20
ν_{13}	0.34	0.34	1.00×10^{-5}
ν_{23}	0.53	0.53	1.00×10^{-5}

Table 1. Material properties for the base, repair, and core

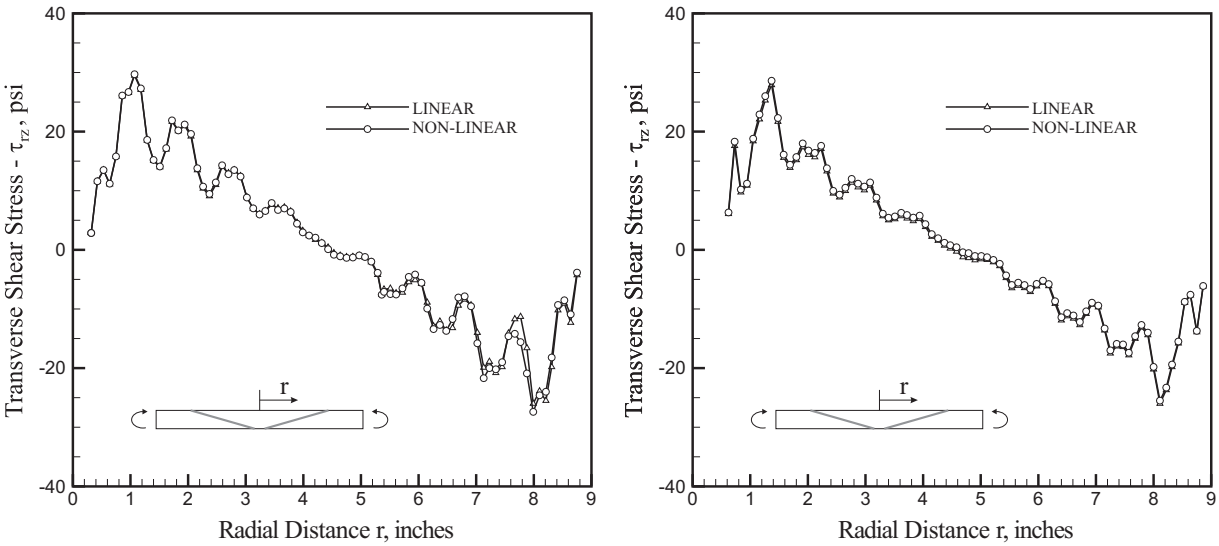

Figure 10. Shear stress, τ_{rz}, variation obtained from (a) the current analysis and (b) ANSYS for a composite panel with a single-sided repair under moment loading.

transverse shear stress inside the adhesive along the x-axis is shown in Figure 10a. The deformations due to the applied loading are not significant enough and therefore there is hardly any difference between the results from the linear and nonlinear analyses. The variation of the transverse shear stress obtained from ANSYS is shown in Figure 10b; the results are in good agreement with the current analysis. In the second case, the laminate is subjected to a moment of $M_x = 10.0$ lbs-in/in along with an in-plane force of $N_x = 100.0$ lbs/in. Even though the panel does not experience large deformations, there is a considerable difference between the solutions obtained from the linear and nonlinear analyses, as shown in Figure 11a. This is due the presence of in-plane forces that introduce the stress stiffening effect, which is not considered in the linear analysis. The results obtained from ANSYS are shown in Figure 11b; they match the results obtained form the current analysis.

A composite laminate with a double-sided repair is considered next. The geometry, stacking sequence, and material properties are same as the previous problem, which involved a laminate with a single-sided repair. The panel is subjected to an in-plane force of $N_x = 1000.0$ lbs/in. The stress variations inside the adhesive along lines that are 0°, 30°, 60°, and 90° from the x-axis are shown in Figures 12a and 12b. Since both the stacking sequence and the nature of the repair are symmetrical, the variations of shear stresses τ_{rz} and $\tau_{\theta z}$ are shown only inside the adhesive layer between the top repair and the base. A dominant peak is observed at the inner edge of the repair, which is also the location where two 0° plies exist. As expected the shear stress, τ_{rz}, is dominant along the direction of loading, that is, the x-axis, whereas the $\tau_{\theta z}$ component has significant stress concentration in the 30°–60° region.

A sandwich panel with full repair of the top face sheet is considered next. The panel has length and width of 40 in and 28 in, respectively. The inner radius of the scarf repair is 0.25 inch, and the scarf ratio is 30.0. The top face sheet has 40 plies with a stacking sequence of $(45/90/-45/0)_{5s}$ and the bottom face sheet has 8 plies with a stacking sequence of $(45/90/-45/0)_2$. Each ply has a thickness of 0.0072 in, and the core is 1.0 in thick. The material properties of the undamaged top and bottom face

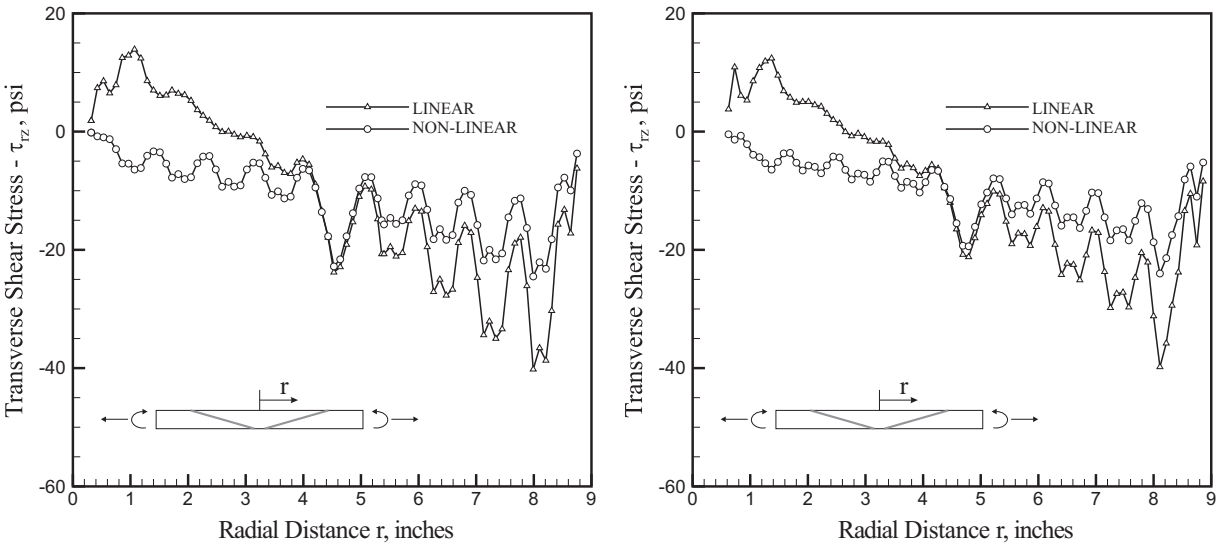

Figure 11. Shear stress, τ_{rz}, variation obtained from (a) the current analysis and (b) ANSYS for a composite panel with a single-sided repair under combined moment and in-plane loading.

sheets correspond to the base material in Table 1. The material properties of the repair and core are also given in Table 1. The adhesive, which is 0.01 in thick, has a bilinear stress-strain relationship. The shear moduli of the adhesive are $G_1 = 6.0 \times 10^4$ psi and $G_2 = 6.0 \times 10^2$ psi, and the Poisson's ratio is $\nu = 0.3$. The adhesive has a critical shear strain values of $\gamma_c = 0.04$. The edge of the sandwich panel

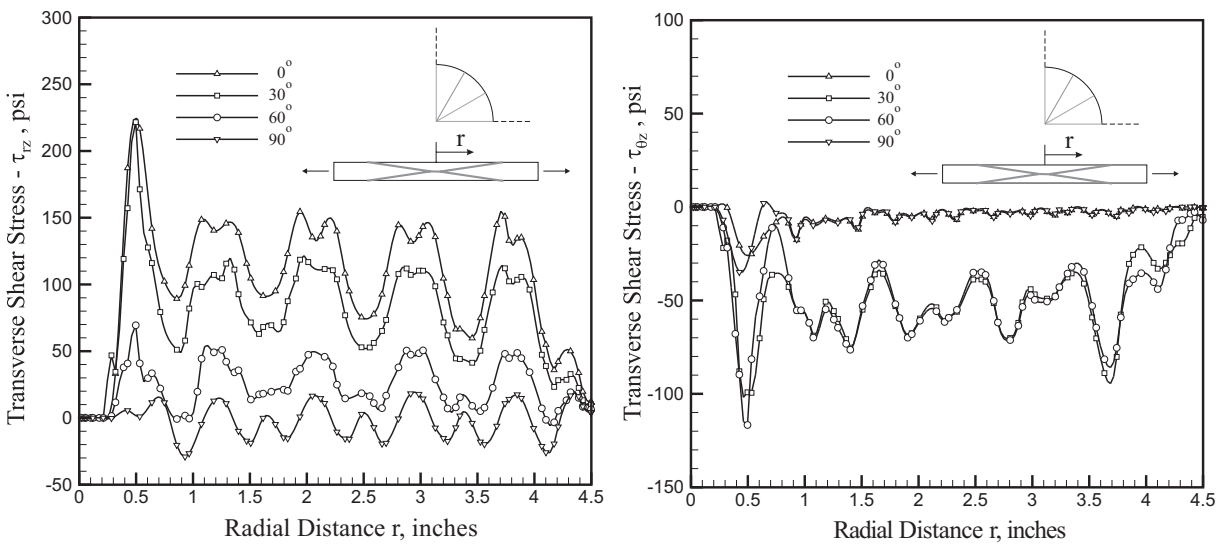

Figure 12. Shear stresses, (a) τ_{rz} and (b) $\tau_{\theta z}$, inside the adhesive between the top repair and base of a composite panel with a double-sided repair.

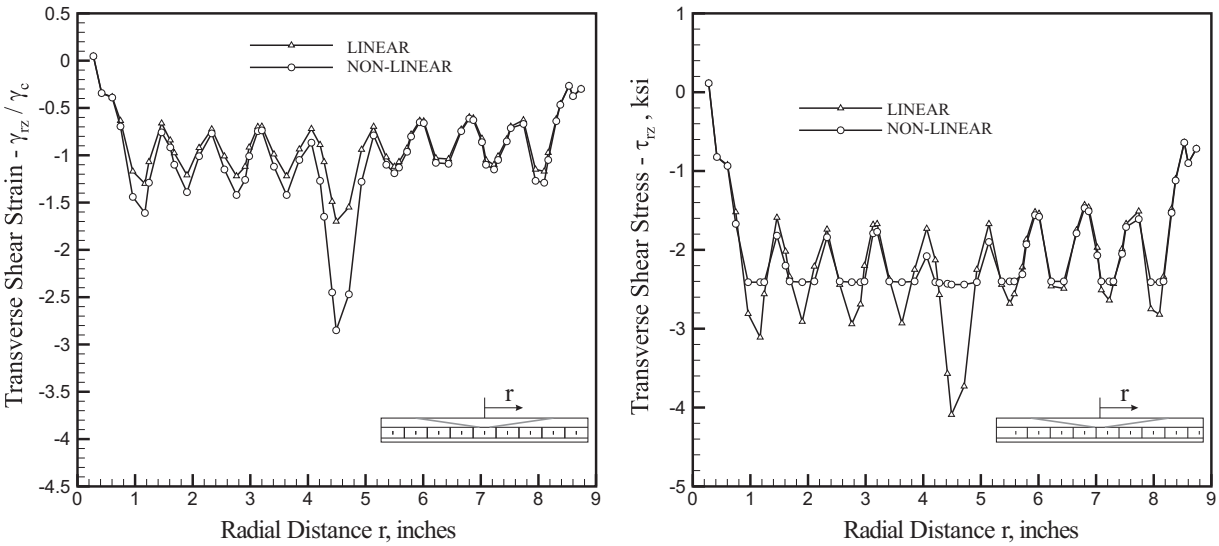

Figure 13. (a) Shear strain, γ_{rz}, and (b) shear stress, τ_{rz}, variations obtained from the current analysis for a sandwich under prescribed displacement.

is subjected to a displacement of $u_x = 0.2$ in. Under the influence of the prescribed displacement, the effective strain inside the adhesive exceeds the critical strain, thereby triggering the nonlinear material response. The transverse shear strain, γ_{rz}, and stress, σ_{rz}, inside the adhesive along the x-axis are shown in Figure 13. Since the effective strain in certain regions exceeds the critical value of $\gamma_c = 0.04$, the elastic modulus in those regions gets degraded. This leads to higher strain values in comparison to the

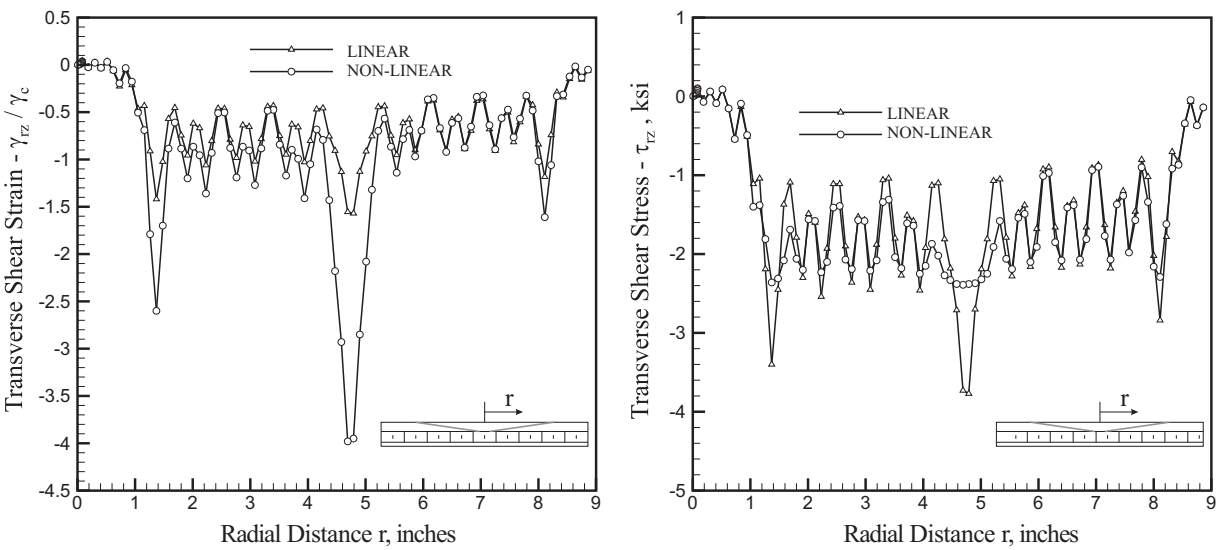

Figure 14. (a) Shear strain, γ_{rz}, and (b) shear stress, τ_{rz}, variations obtained from ANSYS for a sandwich under prescribed displacement.

linear response, reduced stresses in these regions, and an additional load carried by the face sheet in the undamaged region. As shown in Figure 14, the results from ANSYS show a similar trend.

7. Conclusion

An analysis tool for scarf repair analysis of composite laminates and sandwich panels has been developed. Apart from analyzing two-dimensional scarf joints, the current tool can be used for three-dimensional analysis of scarf repair. Composite laminates with single-sided or double-sided repairs and sandwich panels with complete or partial repairs of the top face sheet can be analyzed. The analysis takes into account both geometric and material nonlinearity. The loading, material properties, and panel geometry can be arbitrary. Although computationally efficient, the stress and strain fields can be accurately predicted. Depending on the type and magnitude of loading, there can be a considerable difference between the linear and nonlinear solutions.

References

[Bair et al. 1991] D. L. Bair, P. O. Hudson, and G. R. Ghanimati, "Analysis and repair of damaged composite laminates", pp. 2264–2278 in *How concept becomes reality: 36th International SAMPE Symposium and Exhibition* (San Diego, CA, 1991), vol. 2, edited by J. Stinson et al., SAMPE, Covina, CA, 1991.

[Baker et al. 1999] A. A. Baker, R. J. Chester, G. R. Hugo, and T. C. Radtke, "Scarf repairs to highly strained graphite/epoxy structure", *Int. J. Adhes. Adhes.* **19**:2–3 (1999), 161–171.

[Barut et al. 2001] A. Barut, E. Madenci, J. Heinrich, and A. Tessler, "Analysis of thick sandwich construction by a {3, 2}-order theory", *Int. J. Solids Struct.* **38**:34–35 (2001), 6063–6077.

[Campilho et al. 2007] R. D. S. G. Campilho, M. F. S. F. de Moura, and J. J. M. S. Domingues, "Stress and failure analyses of scarf repaired CFRP laminates using a cohesive damage model", *J. Adhes. Sci. Technol.* **21**:9 (2007), 855–870.

[Carpenter 1973] W. Carpenter, "Finite element analysis of bonded connections", *Int. J. Numer. Methods Eng.* **6**:3 (1973), 450–451.

[Cook and Tessler 1998] G. M. Cook and A. Tessler, "A {3, 2}-order bending theory for laminated composite and sandwich beams", *Compos. B Eng.* **29**:5 (1998), 565–576.

[Das et al. 2005] M. Das, A. Barut, E. Madenci, and D. R. Ambur, "Complete stress field in sandwich panels with a new triangular finite element of single-layer theory", *Comput. Methods Appl. Mech. Eng.* **194**:27–29 (2005), 2969–3005.

[Das et al. 2006] M. Das, A. Barut, E. Madenci, and D. R. Ambur, "A triangular plate element for thermo-elastic analysis of sandwich panels with a functionally graded core", *Int. J. Numer. Methods Eng.* **68**:9 (2006), 940–966.

[Du et al. 2004] J. Du, F. T. Salmon, and A. V. Pocius, "Modeling of cohesive failure processes in structural adhesive bonded joints", *J. Adhes. Sci. Technol.* **18**:3 (2004), 287–299.

[Erdogan and Ratwani 1971] F. Erdogan and M. Ratwani, "Stress distribution in bonded joints", *J. Compos. Mater.* **5**:3 (1971), 378–393.

[Gunnion and Herszberg 2006] A. J. Gunnion and I. Herszberg, "Parametric study of scarf joints in composite structures", *Compos. Struct.* **75**:1–4 (2006), 364–376.

[Harman and Wang 2006] A. B. Harman and C. H. Wang, "Improved design methods for scarf repairs to highly strained composite aircraft structure", *Compos. Struct.* **75**:1–4 (2006), 132–144.

[Hart-Smith 1973] L. J. Hart-Smith, "Adhesive-bonded scarf and stepped-lap joints", report NASA-CR-112237, NASA, 1973, Available at http://tinyurl.com/59wc5s.

[Johnson 1989] C. L. Johnson, "Effect of ply stacking sequence on stress in a scarf joint", *AIAA J.* **27**:1 (1989), 79–86.

[Kumar et al. 2006] S. B. Kumar, I. Sridhar, S. Sivashanker, S. O. Osiyemi, and A. Bag, "Tensile failure of adhesively bonded CFRP composite scarf joints", *Mater. Sci. Eng. B* **132**:1–2 (2006), 113–120.

[Mortensen and Thomsen 1997] F. Mortensen and O. T. Thomsen, "Simplified linear and non-linear analysis of stepped and scarfed adhesive-bonded lap-joints between composite laminates", *Compos. Struct.* **38**:1–4 (1997), 281–294.

[Odi and Friend 2002] R. A. Odi and C. M. Friend, "A comparative study of finite element models for the bonded repair of composite structures", *J. Reinf. Plast. Compos.* **21**:4 (2002), 311–332.

[Soutis and Hu 1997] C. Soutis and F. Z. Hu, "Repair design of composites and efficiency of scarf patch repairs", pp. 395–404 in *Proceedings of the 11th International Conference on Composite Materials (ICCM-11)* (Gold Coast, Queensland), vol. VI, edited by M. L. Scott, Woodhead Publishing, Cambridge, 1997.

[Tomblin et al. 2004] J. S. Tomblin, L. Salah, J. M. Welch, and M. D. Borgman, "Bonded repair of aircraft composite sandwich structures", Report DOT/FAA/AR-03/74, US FAA, 2004, Available at http://www.tc.faa.gov/its/worldpac/techrpt/ar03-74.pdf.

[Wang and Gunnion 2008] C. H. Wang and A. J. Gunnion, "On the design methodology of scarf repairs to composite laminates", *Compos. Sci. Technol.* **68**:1 (2008), 35–46.

Received 29 Apr 2008. Revised 4 Sep 2008. Accepted 11 Sep 2008.

MANABENDRA DAS: mdas@email.arizona.edu
Department of Aerospace and Mechanical Engineering, The University of Arizona, 1130 N. Mountain Avenue, Tucson, AZ 85721, United States

ERDOGAN MADENCI: madenci@email.arizona.edu
Department of Aerospace and Mechanical Engineering, The University of Arizona, 1130 N. Mountain Avenue, Tucson, AZ 85721, United States

DAMODAR R. AMBUR: damodar.r.ambur@nasa.gov
Research and Technology Directorate, NASA Langley Research Center, Hampton, VA 23681-2199, United States